Nano Research 2016, 9(1): 117–127
DOI 10.1007/s12274-015-0892-x
Research Article
ISSN 1998-0124
CN 11-5974/O4

Thermoelectric properties of solution-synthesized n-type Bi_2Te_3 nanocomposites modulated by Se: An experimental and theoretical study

Haiyu Fang[1,†], Je-Hyeong Bahk[2,‡], Tianli Feng[3], Zhe Cheng[4], Amr M. S. Mohammed[2], Xinwei Wang[4], Xiulin Ruan[3], Ali Shakouri[2], and Yue Wu[5] (✉)

[1] *School of Chemical Engineering, Purdue University, West Lafayette, IN 47907, USA*
[2] *Birck Nanotechnology Center, Purdue University, West Lafayette, IN 47907, USA*
[3] *School of Mechanical Engineering, Purdue University, West Lafayette, IN 47907, USA*
[4] *Department of Mechanical Engineering, Iowa State University, Ames, IA 50011, USA*
[5] *Department of Chemical and Biological Engineering, Iowa State University, Ames, IA 50011, USA*
[†] *Present address: Materials Research Laboratory, UC Santa Barbara, Santa Barbara, CA 93106, USA*
[‡] *Present address: Department of Mechanical and Materials Engineering, University of Cincinnati, Cincinnati, OH 45221, USA*

Received: 20 July 2015
Revised: 18 August 2015
Accepted: 5 September 2015

KEYWORDS
Bi_2Te_3,
Se doping,
solution synthesis,
nanostructure,
thermoelectric

ABSTRACT

We report the investigation of the thermoelectric properties of large-scale solution-synthesized Bi_2Te_3 nanocomposites prepared from nanowires hot-pressed into bulk pellets. A third element, Se, is introduced to tune the carrier concentration of the nanocomposites. Due to the Se doping, the thermoelectric figure of merit (ZT) of the nanocomposites is significantly enhanced due to the increased power factor and reduced thermal conductivity. We also find that thermal transport in our hot-pressed pellets is anisotropic, which results in different thermal conductivities along the in-plane and cross-plane directions. Theoretical calculations for both electronic and thermal transport are carried out to establish fundamental understanding of the material system and provide directions for further ZT optimization with adjustments to carrier concentration and mobility.

1 Introduction

Bismuth telluride (Bi_2Te_3) materials have remained the best thermoelectric materials for use at room temperature for many decades since the 1960s. The efficiency of a thermoelectric device is directly related to the thermoelectric figure of merit, defined as $ZT = S^2\sigma T/\kappa$, where S is the Seebeck coefficient, σ is the electrical conductivity, κ is the thermal conductivity and T is the absolute temperature. Typically, the best

Address correspondence to yuewu@iastate.edu

ZT values of single-crystalline Bi_2Te_3 ingots alloyed with Sb (p-type) and Se (n-type) are around 1 [1–3]. In the past decade, researchers have begun to fabricate nanostructured Bi_2Te_3, which shows enhanced ZT that benefit from the reduction of thermal conductivity caused by increased phonon scattering at the interfaces and grain boundaries. One highly cited example is $Bi_{0.5}Sb_{1.5}Te_3$ nanostructured bulk material with a ZT value of 1.4 [4]. This success has encouraged a great deal of research efforts focused on similar nanostructured materials. However, complex high-vacuum molecular beam epitaxy and energy-intensive ball milling were involved in fabricating those materials, making the process complex and costly. Therefore, solution synthesis of nanostructured Bi_2Te_3, as an alternative path toward cost-effective and energy-efficient material production, is worth further study. Mehta and coworkers reported that solution-synthesized n-type Bi_2Te_3 and p-type $Bi_{0.5}Sb_{1.5}Te_3$ nanoplates achieved ZT values of 1.1 and 1.2, respectively, which is the most successful effort to date in solution-synthesized nanostructured Bi_2Te_3 [5]. However, the scalability of solution synthesis has not been demonstrated to a satisfactory degree in the literature. Recently, our group reported a 1 L scale synthesis of Bi_2Te_3 nanowires, in which over 17 g of Bi_2Te_3 nanowires were produced at an impressive yield of 94.21% [6], which provides enough nanopowder to make tens of pellets through hot press methods. The scaled up reaction provides a platform where the thermoelectric performance of solution-synthesized Bi_2Te_3 can be thoroughly investigated by tuning various material parameters, such as carrier concentration, mobility and so on, without needing the time to synthesize multiple batches. In addition, measuring samples from the same batch minimizes the variation of materials properties that are present among different batches.

Bi_2Te_3 has a layered lattice structure, and the configuration of one quantum layer is Te(1)–Bi–Te(2)–Bi–Te(1) as shown in Fig. 1(a). Te(1) and Bi are covalently bonded while adjacent quantum layers are loosely bonded thorough Van der Waals forces [7, 8]. Due to this unique crystal structure, the defect chemistry of Bi_2Te_3 is quite complicated. Te vacancy is one of

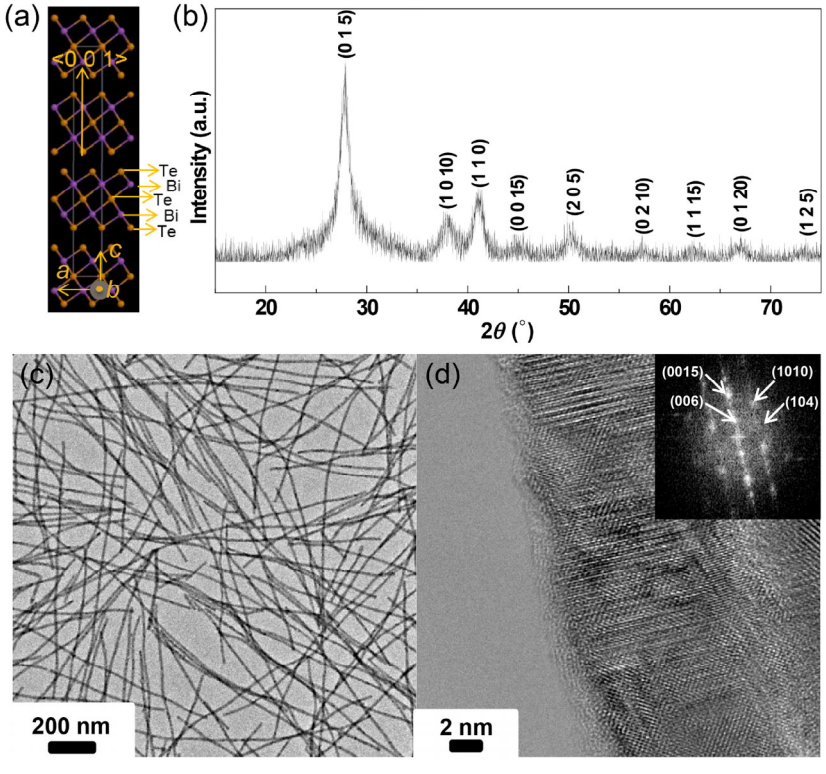

Figure 1 (a) The scheme of Bi_2Te_3 lattice; the picture is from Jmol (an open-source Java viewer for chemical structures in 3D; http://www.jmol.org/). (b) The XRD pattern of as-synthesized Bi_2Te_3 nanowires. (c) The low-resolution TEM image of Bi_2Te_3 nanowires and (d) the HRTEM image of one Bi_2Te_3 nanowire with the inset being the FFT of the selected area.

the most common defects existing in Bi_2Te_3. Since Te (52.55 kJ·mol^{-1}) has a smaller evaporation energy than Bi (104.80 kJ·mol^{-1}), Te tends to evaporate more readily than Bi during high temperature consolidation or annealing [9]. A single Te vacancy can donate two free electrons according to the reaction $Te_{Te} = V_{Te}^{2+} + Te + 2e^-$, which significantly increases n-type conductance [10–12]. Due to the small electronegativity difference between Bi and Te [13], anti-site defects of Bi occupying Te site (Bi_{Te}) and Te occupying Bi site (Te_{Bi}) are also widely found in Bi_2Te_3. The formation of a Bi_{Te} antisite defect follows the reaction $Bi + Te_{Te} = Bi_{Te}^- + Te + h^+$ and donates one free hole to the matrix per site [14–16]. A Te_{Bi} antisite defect, on the other hand, donates one free electron to the matrix per site following the reaction $Te + Bi_{Bi} = Te_{Bi}^+ + Bi + e^-$ [13, 17]. Recent reports show that the Seebeck coefficient of Bi_2Te_3 nanowires is much lower than that of bulk material, mainly due to the higher carrier concentration contributed by antisite defects. These defects are more easily formed in Bi_2Te_3 nanowires, most likely due the dangling bonds on the large surface area [18–20]. It is found that the consolidated pellets of our large-scale synthesized Bi_2Te_3 nanowires have extremely high carrier concentrations, so Se was used as a dopant to occupy the double-charged Te vacancies and provide free electrons. Another important parameter that often receives less attention is the carrier mobility in nanostructured thermoelectric materials. Theoretical work based on our experimental results reveals that mobility is just as important as carrier concentration in designing thermoelectric materials. Achieving the best ZT value depends on the simultaneous optimization of both carrier concentration and mobility. Here, a combined experimental and theoretical investigation provides a thorough understanding of solution-synthesized Bi_2Te_3 materials systems.

2 Experimental

The synthesis of Bi_2Te_3 nanowires exactly follows the procedure in our previously published paper on the large-scale production of Bi_2Te_3 nanowires [6]. After the as-synthesized Bi_2Te_3 nanowires were washed three times with deionized (DI) water, they were re-dispersed and stirred overnight in an aqueous hydrazine solution composed of 90% of water and 10% of hydrazine hydrate solution (80%) in order to eliminate leftover surfactants on the nanowires. Then, the Bi_2Te_3 nanowires were washed three times with DI water and once with ethanol before drying under vacuum and annealing at 450 ℃ for 30 min. Afterwards, the Bi_2Te_3 nanowires were ground into a fine powder in a glovebox under nitrogen, after which Se powder was thoroughly mixed with the nanowires by grinding. Finally, the mixture was consolidated into centimeter pellets and hot-pressed at 450 ℃ for 30 min.

3 Results and discussion

3.1 Material characterization

The as-synthesized Bi_2Te_3 nanowires are characterized using X-ray diffraction (XRD) and transmission electron microscopy (TEM) (Fig. 1). The XRD spectrum of the nanowires can be readily indexed as Bi_2Te_3 (JCPDS No. 15-0863) without any impurity peaks identified (Fig. 1(b)). The low-resolution TEM image shows the morphology of nanowires with uniform distribution (Fig. 1(c)). The lattice-resolved image of a single nanowire was obtained using high-resolution TEM (HRTEM) (Fig. 1(d)), which reveals the polycrystalline nature of the nanowire while the fast Fourier transformation is indexed as a pure Bi_2Te_3 phase. More discussion on the Bi_2Te_3 nanowire characterization can be found in our previous report [6].

A total of seven different pellets with different Se concentrations were fabricated to study carrier concentration optimization. First, the densities of these Bi_2Te_3 nanocomposite pellets were calculated from the mass and the sample dimensions, and the theoretical density of Bi_2Te_3 was used for the relative density calculation. The results listed in Table 1 indicate that all of the pellets possess high relative densities over 90%. Furthermore, the Se concentration in each pellet was measured with energy-dispersive X-ray spectroscopy (EDS), with error bars arising from the geometrical distribution of Se (Table 1). The corresponding chemical formula based on the EDS results for each pellet is also summarized in Table 1.

Table 1 A summary of the relative density, Se atomic percentage and chemical formula of all the samples identified by numbers from 1 to 7

Sample ID	Relative density (%)	Se atomic %	$Bi_2Te_xSe_y$
1	92.42	0	$Bi_2Te_{2.62}$
2	92.81	1.52 ± 0.34	$Bi_2Te_{2.62}Se_{0.07}$
3	92.49	3.91 ± 0.68	$Bi_2Te_{2.64}Se_{0.19}$
4	90.57	5.66 ± 0.58	$Bi_2Te_{2.57}Se_{0.27}$
5	90.44	8.20 ± 0.97	$Bi_2Te_{2.51}Se_{0.4}$
6	91.95	11.54 ± 0.68	$Bi_2Te_{2.42}Se_{0.58}$
7	91.34	17.71 ± 0.38	$Bi_2Te_{2.14}Se_{0.89}$

Notably, the Se concentration has a significant impact on the XRD spectra of the pellets as shown in Fig. 2(a). Te and Se are in the same group in the periodic table, but Se has a smaller atomic radius than Te. Therefore, Se doping decreases the lattice constants and causes the XRD peaks to shift to larger angles according to the Bragg equation ($\sin\theta = n\lambda/2d$). The initial observation on the XRD spectra shown in Fig. 2(a) confirms this. Moreover, the lattice constant a calculated from the XRD spectra decreases as the Se concentration decreases (Fig. 2(c)). However, the (006) peak position in Fig. 2(b), which is solely determined by the c constant, shifts to a smaller angle and then to a larger angle as the Se concentration increases. The calculated lattice constant c corresponds to the (006) peak shifting and reaches a maximum value of 30.229 Å, which is a smaller value than that of pure Bi_2Te_3 (30.483 Å) at a Se concentration of 3.91%. Combining the EDS results (Table 1) and the fact that a monotonically decreases while c first increases and then decreases with Se concentration (Fig. 2(d)), we propose a plausible Se doping mechanism that explains the variation of the lattice constants and carrier concentration with Se concentration that was measured later on.

Sample 1, which is prepared from pure Bi_2Te_3 nanowires with no Se, is found to be Te deficient (Table 1), which means there are a large number of Te vacancies present in the lattice. As shown earlier in Fig. 1(a), since Bi_2Te_3 has a layered lattice structure, the existence of a large number of Te vacancies implies that some Te atomic layers are missing in the lattice, which leads to a smaller c constant (29.891 Å) than that of perfect crystalline Bi_2Te_3 (30.483 Å), whereas the a constant (4.409 Å) is slightly higher than that of perfect crystalline Bi_2Te_3 (4.385 Å) because Bi has a larger atomic radius than Te. When Se is doped into the Bi_2Te_3 pellets, Te vacancies are occupied by Se, which causes the layer structure to stretch along the c

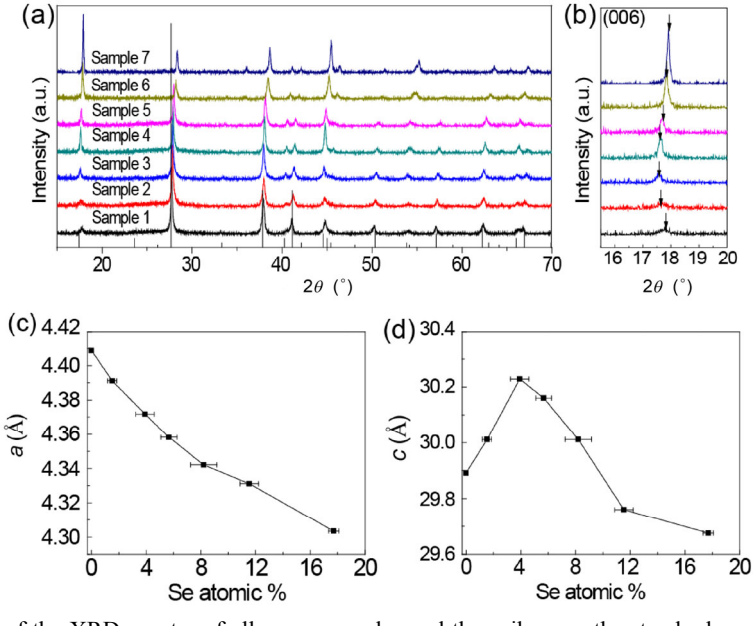

Figure 2 (a) The summary of the XRD spectra of all seven samples and the spikes are the standard spectrum of Bi_2Te_3 (JCPDS No. 15-0863). (b) The (006) peaks of the samples. (c) and (d) The change of calculated lattice constants a and c with Se atomic percentage, respectively.

direction, leading to a larger *c* constant. However, the *a* constant becomes smaller because Se has a much shorter atomic radius than Bi and Te. As Se concentration increases past 3.91%, the *c* constant starts to decrease while the *a* constant continues to decrease. At this point, Se not only fills the Te vacancies but also begins to occupy the Bi atomic layers to form Se_{Bi} antisites or even replacing Te, likely due to the defect formation energy of Se_{Bi} antisites being more favorable with greater Se content or lesser Bi content [13]. Again, due to the difference in atomic radii between Bi and Se, the layer structure shrinks in the *c* direction, leading to a lower *c* constant, while the *a* constant continues its decreasing trend.

3.2 Electrical properties with varying Se concentration

Figure 3 shows how Se concentration influences the electrical properties of the samples at 300 K. As discussed earlier, each Te vacancy donates two electrons, so sample 1 with no Se has an extremely high carrier concentration of 5.36×10^{20} cm^{-3} (Fig. 3(a)). When Se is doped into the system, samples 2 and 3 possess reduced carrier concentrations because Se occupies the Te vacancies and compensates the two free electrons following $Se + V_{Te}^{2+} + 2e^- = Se_{Te}$, which decreases the carrier concentration in the material. The Se doping efficiency is calculated to be 0.45 electrons per Se atom from the results of samples 1–3. Interestingly, the carrier concentration reaches a minimum value of 2.84×10^{19} cm^{-3} in sample 3 at 3.9% Se and then starts to increase, which exactly corresponds to the crest point of the *c* constant as shown in Fig. 2(d). As discussed in the Se doping mechanism, Se occupies the Bi site, which donates one free electron to the system according to $Se + Bi_{Bi} = Se_{Bi}^{+} + Bi + e^-$. The Se doping efficiency is calculated to be 0.11 electrons per Se atom from the results of samples 3–5. As Se concentration further increases, sample 6 has almost identical carrier concentration as sample 5 at 1.60×10^{20} cm^{-3}, whereas the carrier concentration of sample 7 drops to 1.10×10^{20} cm^{-3}. The EDS results show that Se starts to replace Te beginning in sample 5 (Te concentration decreases with Se concentration from samples 5 to 7). Se_{Te} would not influence the carrier concentration but since the band gap of $Bi_2Te_{3-x}Se_x$ increases linearly with increasing Se content [21] (Fig. 3(b)), which could explain why the carrier concentration goes through a plateau before a relatively small drop at higher Se concentrations. Note that

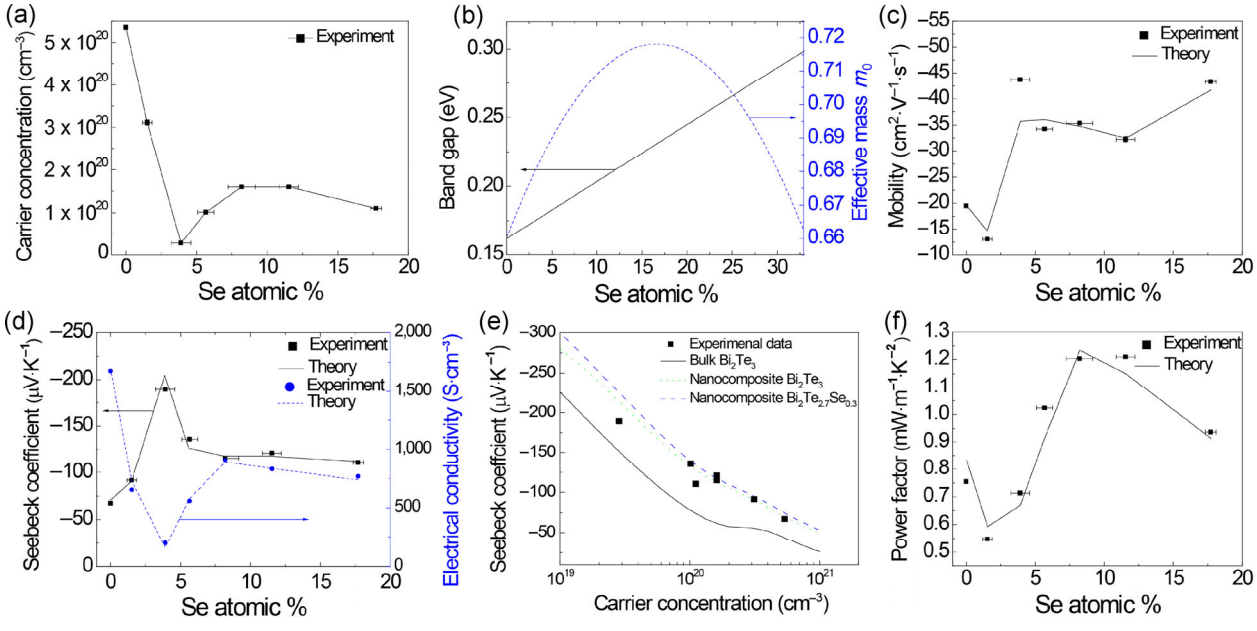

Figure 3 Influence of Se concentration on thermoelectric properties at 300 K. (a) Carrier concentration; (b) the theoretical calculation result of band gap and effective mass; (c) mobility; (d) Seebeck coefficient and electrical conductivity; (e) Pisarenko relation (Seebeck coefficient vs. carrier concentration); (f) power factor.

the band gap may vary due to the large amount of Te vacancies and Se atoms occupying Te and Bi sites in the samples, but the theoretical calculation results obtained with the band gap values in Fig. 3(b) still agree with the experimental data well. Figure 3(c) shows the electron mobility of the samples at 300 K, which reveals a few important points. First, the magnitude of the mobility is in the range from 12 to 45 $cm^2 \cdot V^{-1} \cdot s^{-1}$ which is comparable to some other solution-synthesized $Bi_2Te_{3-x}Se_x$ nanocomposites [22–24] and thin films [25–27], but smaller than most mechanically alloyed [9, 28] and single crystalline $Bi_2Te_{3-x}Se_x$ [2], in which the mobility is about one order of magnitude higher, being from 100 to 250 $cm^2 \cdot V^{-1} \cdot s^{-1}$. Second, our theoretical calculation results show that a scattering parameter (r) of 0.8 is extracted from the fitting of the mobility and the Seebeck coefficient, compared to the much smaller scattering parameter found for the bulk material (r = –0.3 to 0.5), which is due to the increased ionized defect scattering at grain boundaries in these nanocomposites.

The influence of Se concentration on Seebeck coefficient and electrical conductivity at 300 K is shown in Fig. 3(d). All the samples have negative Seebeck coefficients, which indicate their n-type doping. The Seebeck coefficient generally follows the Mott relation, in which a higher carrier concentration leads to a lower Seebeck coefficient (Fig. 3(d)) [29, 30]. The highest Seebeck coefficient (–189 $\mu V \cdot K^{-1}$) was achieved at a Se concentration of 3.91%, which corresponds to the carrier concentration of 2.84 × 10^{19} cm^{-3}, while the lowest Seebeck coefficient (–67 $\mu V \cdot K^{-1}$) was measured in sample 1 with the carrier concentration of 5.36 × 10^{20} cm^{-3} (Fig. 3(d)). A theoretical study based on the Boltzmann transport equations was performed to calculate the Pisarenko relation (carrier concentration vs. Seebeck coefficient) as shown in Fig. 3(e). The Seebeck coefficients of all the samples are found to be above the bulk curve, which means our nanocomposites possess higher magnitudes of Seebeck coefficient than bulk material at equivalent carrier concentrations. The enhancement of the Seebeck coefficients is attributed to the increased ionized defect scattering at grain boundaries in the nanocomposites as discussed previously. The electrical conductivities of all the samples at 300 K are also shown in Fig. 3(d). Generally, the electrical conductivity follows the same trend as the carrier concentration with varying Se content. The highest electrical conductivity is found to be 1,675 $S \cdot cm^{-1}$ in sample 1 while the lowest electrical conductivity is 198 $S \cdot cm^{-1}$ obtained at a Se concentration of 3.91% in sample 3. Overall, the reduced mobility of our samples leads to smaller electrical conductivities than those of the mechanically alloyed samples [9, 28] or single crystalline $Bi_2Te_{3-x}Se_x$ at the equivalent carrier concentration [2]. However, the electrical conductivities of our samples are higher than those of some other solution synthesized $Bi_2Te_{3-x}Se_x$ nanocomposites [22–24].

Based on the Seebeck coefficient and electrical conductivity at 300 K, the power factor was calculated and plotted in Fig. 3(f). A maximum power factor of ~1.2 $mW \cdot m^{-1} \cdot K^{-2}$ is obtained when the Se concentration is 8.2%–11.54% with a carrier concentration of ~1.60 × 10^{20} cm^{-3}. Note that the mechanically alloyed $Bi_2Te_{3-x}Se_x$ reported in Refs. [9, 28] achieved maximum power factors at carrier concentrations of 1.50 × 10^{19} and 2.28 × 10^{19} cm^{-3}, respectively. These carrier concentrations are about an order of magnitude lower than the optimal carrier concentration obtained from our samples. This is due to the relatively lower mobility of our samples, which makes the optimal carrier concentration shift to a higher value [29]. Meanwhile, another case of solution-synthesized $Bi_2Te_{3-x}Se_x$ nanocomposites claims that the optimal power factor was obtained at a much higher carrier concentration of 7.8 × 10^{20} cm^{-3} and the corresponding mobility was 1.33 $cm^2 \cdot V^{-1} \cdot s^{-1}$ [24].

Figure 4 shows the temperature dependent thermoelectric properties of the $Bi_2Te_{3-x}Se_x$ nanocomposites. On one hand, the negative temperature dependent behavior of electrical conductivity of almost all the samples indicates they are degenerate semiconductors except for sample 3, which shows a positive temperature coefficient ($d\sigma/dT$) due to its low carrier concentration (Fig. 4(a)). We also note that the peak Seebeck coefficient shifts from 480 K in sample 1 to 400–440 K in the other samples because the reduced carrier concentration by Se doping decreases the onset temperature of the bipolar effect (Fig. 4(b)) [31]. The power factor is plotted in Fig. 4(c). Due to the decrease in Seebeck coefficient with temperature,

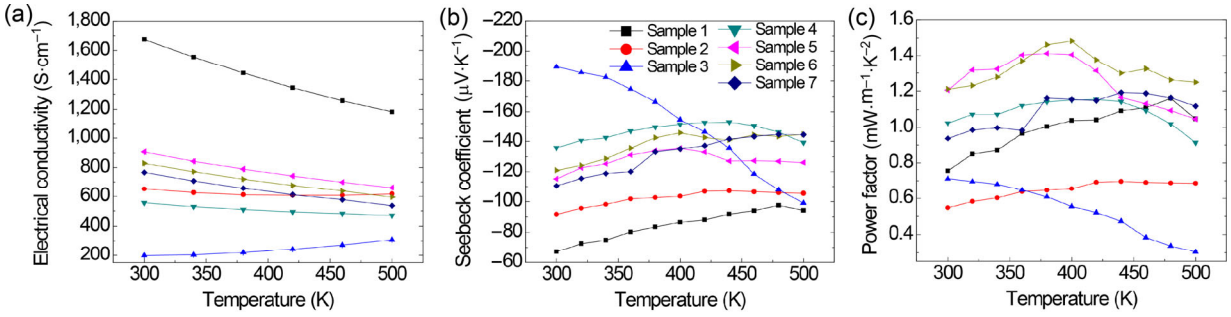

Figure 4 The temperature dependent thermoelectric properties. (a) Electrical conductivity; (b) Seebeck coefficient; (c) power factor.

sample 3 has the lowest power factor among the samples. Also, in the temperature range of 300–500 K, the optimal Se concentration is 11.54%, which gives the highest power factor of 1.48 $mW \cdot m^{-1} \cdot K^{-2}$ at 400 K. This value is much higher than that of the pure Bi_2Te_3 (no Se) nanocomposite (1.04 $mW \cdot m^{-1} \cdot K^{-2}$ at 400 K and 1.16 $mW \cdot m^{-1} \cdot K^{-2}$ at 480 K). This enhancement is attributed to the optimized carrier concentration and increased mobility.

3.3 Anisotropic thermal conductivity and ZT

In order to investigate the anisotropy of the thermal conductivity, which is expected due to the highly anisotropic lattice structure of $Bi_2Te_{3-x}Se_x$ (Fig. 1(a)), the thermal conductivity was measured along two different directions, in-plane and cross-plane, at 300 K. The measurement results (Fig. 5(a)) show that the in-plane thermal conductivity is around two times higher than the cross-plane thermal conductivity. The scanning electron microscopy (SEM) images of the pellet cross sections reveal the laminated structure after hot pressing, which explains the anisotropic thermal transport in the support information (Fig. S1 in the Electronic Supplementary Material (ESM)). The anisotropic thermal transport is thought to be caused by the hot pressing process, because the set-up used in this research has a slow ramping speed (~5 $K \cdot min^{-1}$) and an even slower cooling speed (~1 $K \cdot min^{-1}$). This significantly extends the time when the samples were kept at high temperatures, which leads to the regrowth of Bi_2Te_3 crystals. The regrown crystals preferably form laminates that stack in the direction of the applied pressure, which is the cross-plane direction of the pellets. As Bi_2Te_3 has a layered lattice structure, the cross-plane direction of the laminate-like crystals in the pellets may be along the *c* axis, where the thermal conductivity of Bi_2Te_3 is the smallest since the quantum layers are connected with Van der Waals forces (Fig. 1(a)). Therefore, a much smaller thermal conductivity is observed in the cross-plane direction than the in-plane direction of the pellets. To minimize the regrowth, spark plasma sintering is preferred, since it has a fast ramping and cooling speed, which ensures that the samples do not stay at high temperatures for too long during dense pellet formation [32]. Another interesting aspect is that the thermal conductivity decreased significantly with increasing Se content, which is mainly due to the reduced electronic thermal conductivity. The electronic and lattice contributions to the in-plane thermal conductivity are also calculated and plotted in Fig. 5(a). The lattice thermal conductivity first increases and then decreases with Se concentration, which could be caused by the defects in the samples. In sample 1, there is a large number of Te vacancies and these defects are compensated by Se occupation after Se doping, so from samples 1 to 3, the lattice thermal conductivity increases with Se concentration. However, after sample 3, the new defects, Se_{Te} antisites, start to form and reduce the lattice thermal conductivity. The temperature dependent cross-plane thermal conductivity can be found in Fig. S2 (in the ESM). The temperature dependent in-plane thermal conductivity was not measured because of instrumental limitations. Since the electrical properties were measured along the in-plane direction, the in-plane thermal conductivity was used to calculate ZT, shown in Fig. 5(b). The ZT is enhanced via Se doping by 3× and peaks at a Se concentration of ~11%. The increase in power factor and reduction in thermal conductivity from Se doping both contribute to the ZT improvement.

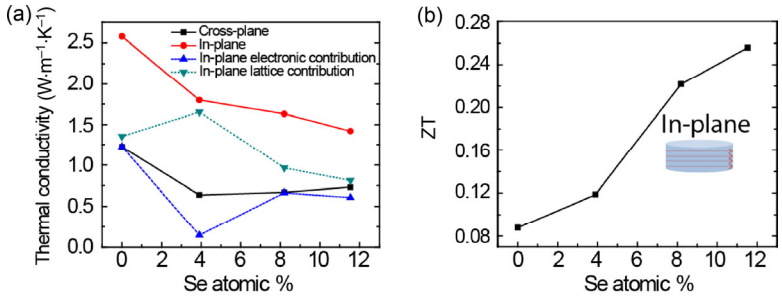

Figure 5 (a) The in-plane and cross-plane thermal conductivity at different Se concentration; the in-plane electronic and lattice contribution are also plotted. (b) ZT at different Se concentration using in-plane properties. The properties were measured at 300 K.

3.4 Further ZT optimization with theoretical modelling

One of the important material parameters that limit ZT in our nanocomposites is their low mobility. Reduced mobility in nanostructured materials is not unusual; it is found in other solution-synthesized nanostructured n-type Bi_2Te_3 [22–24]. Here, we performed a theoretical study to investigate the impact of mobility enhancement on the figure of merit at a given carrier concentration in $Bi_2Te_{2.5}Se_{0.5}$. Three different carrier concentrations, i.e. 2×10^{19}, 9×10^{19}, and 1.6×10^{20} cm^{-3}, were considered for this study, and the mobility was varied by reducing the carrier scattering strength at each carrier concentration. The results of the calculated transport properties as a function of mobility are shown in Fig. 6. We scanned the mobility from the measured value in our samples up to the bulk value at each carrier concentration.

As shown in Fig. 6(b), the power factor increases rapidly with mobility due to the improved electrical conductivity (Fig. 6(a)), and then rolls over as the mobility further increases due to the reduced Seebeck coefficient (Fig. 6(a)) as shown for the carrier concentration of 9×10^{19} cm^{-3}. In general, at a lower mobility, a higher carrier concentration leads to a better power factor; however, at a high mobility, a lower carrier concentration results in a better power factor (Fig. 6(b)).

Thermal conductivity typically consists of electronic, lattice and bipolar contributions, with the last component being negligible at room temperature for Bi_2Te_3 [33]. The electronic contribution of thermal conductivity κ_e was calculated using the Wiedemann-Franz relation with the Lorenz number (L) of 2.44×10^{-8} $W \cdot \Omega \cdot K^{-2}$. The lattice thermal conductivity κ_l as a function of mobility was obtained by assuming that the mobility is tuned by grain size, e.g. electron grain boundary scattering (see the ESM). The estimated grain diameter for samples 5 and 6 is around 4.35 nm, which is larger than the effective phonon mean free path ~2.4 nm but much smaller than the effective electron mean free path ~24 nm in bulk Bi_2Te_3 with 10% Se with carrier concentration of 1.6×10^{20} cm^{-3} (see the ESM). As a consequence, the lattice thermal conductivity does not increase as significantly as the electronic thermal conductivity with mobility, as shown in Fig. 6(c). The increases of the lattice and the electronic thermal conductivities are around 50% and 350%, respectively, from the sample nanostructure to the corresponding bulk for the carrier concentration of 1.6×10^{20} cm^{-3}. As a result, the electronic thermal conductivity is responsible for the greatest portion of the total thermal conductivity at high mobility.

Nanostructuring benefits the value of ZT in these nanocomposites only when the lattice contributes a small portion to the total thermal conductivity. The effect of nanostructuring can be understood explicitly from the ZT expression of $S^2T/(LT+\kappa_l/\sigma)$, where S^2 increases moderately with nanostructuring (or lowering mobility), and κ_l/σ increases rapidly due to the fast decreasing σ. As a result, the dependence of ZT on nanostructuring is determined by whether the lattice of the electron dominates the thermal conductivity. At a higher value of mobility (light nanostructuring), $\kappa_e > \kappa_l$, and ZT increases with nanostructuring mainly due to the increase of S^2 in the numerator. However, at a lower mobility (heavy nanostructuring), $\kappa_e < \kappa_l$, and ZT decreases with nanostructuring because the fast increase of κ_l/σ overwhelms the moderate increase of S^2. Therefore,

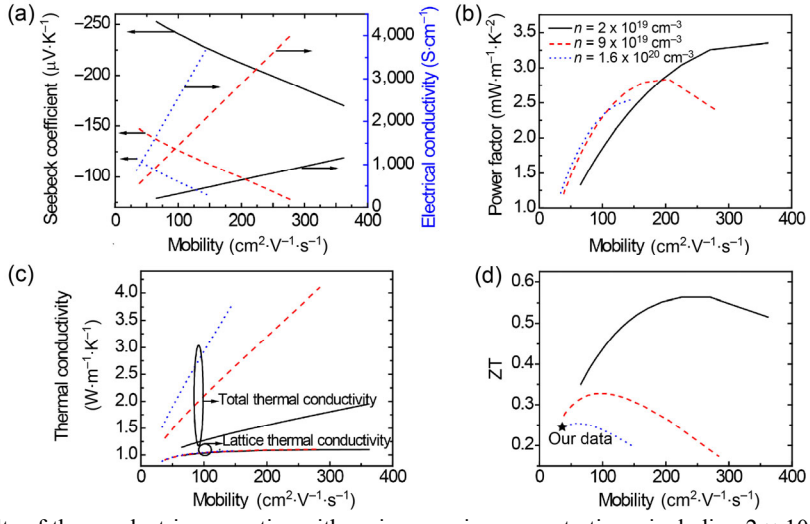

Figure 6 Modeling results of thermoelectric properties with a given carrier concentrations, including 2×10^{19} cm^{-3}, 9×10^{19} cm^{-3} and 1.6×10^{20} cm^{-3}, with varied mobility at 300 K. (a) Seebeck coefficient and electrical conductivity; (b) power factor; (c) thermal conductivity; (d) ZT.

nanostructuring is not always beneficial for ZT, which actually has a maximum value at a certain mobility level that is dependent on carrier concentration (Fig. 6(d)).

Moreover, since a larger carrier concentration leads to higher electronic thermal conductivity (Fig. 6(c)), the highest ZT is found at a relatively low carrier concentration, i.e. 2×10^{19} cm^{-3} in this case as shown in Fig. 6(d). At a high carrier concentration of 1.6×10^{20} cm^{-3}, nanostructuring can be beneficial when it leads to a smaller mobility, as it reduces the electronic thermal conductivity and maximizes ZT at a low mobility as shown in Fig. 6(d). In fact, our material at this carrier concentration has a mobility quite close to the optimal value (marked as "star" in Fig. 6(d)). However, the highest observed ZT of 0.56 is predicted to occur at a carrier concentration of 2×10^{19} cm^{-3} when the mobility is as high as 240 cm^2·V^{-1}·s^{-1}. This is very close to the optimal values (n = (1~2) × 10^{19} cm^{-3} and mobility ~250 cm^2·V^{-1}·s^{-1} for n-type $Bi_2Te_{3-x}Se_x$ ($0 \leqslant x \leqslant 1$). These calculated ZT values shown in Fig. 6(d) provide guidelines in designing nanocomposite materials based on $Bi_2(Te,Se)_3$. Note that these modelling results are based on $Bi_2Te_{2.5}Se_{0.5}$ so the results can vary depending on the material composition.

4 Conclusion

In this paper, Bi_2Te_3 nanowires were solution-synthesized at a large scale of approximately 17 g per batch. The consolidated Bi_2Te_3 nanocomposites have extremely high carrier concentrations, so Se is doped to optimize the carrier concentration. The doping mechanism of Se was studied using XRD and Hall effect measurements, and it is found that Se doping effectively decreases carrier concentration, which leads to an improved power factor and reduced thermal conductivity. Therefore, the ZT is greatly enhanced up to 0.26 at 300 K because of the optimal Se doping at ~11%. Theoretical studies with both electron and thermal transport calculations reveal that this ZT can be further enhanced up to 0.56 when the mobility and the carrier concentration can be simultaneously optimized.

Acknowledgements

H. Y. F. thanks Scott Finefrock and Tianyue Gao for the help in Hall measurement. H. Y. F. and Y. W. acknowledge the use of the hot press setup in Prof. Chin-The Sun's lab at Purdue University. H. Y. F. and Y. W. acknowledge Air Force Office of Scientific Research (No. FA9550-12-1-0061). T. L. F. and X. L. R. acknowledge the partial support from National Science Foundation (No. 1150948).

Electronic Supplementary Material: Supplementary material (details of experiments and procedures for the theoretical, SEM images of the cross section of hot pressed pellets, temperature dependent cross section

thermal conductivity and schematic of the experimental setup for characterizing the in-plane thermal conductivity) is available in the online version of this article at http://dx.doi.org/10.1007/s12274-015-0892-x.

References

[1] Yim, W. M.; Rosi, F. D. Compound tellurides and their alloys for peltier cooling—A review. *Solid-State Electron.* **1972**, *15*, 1121–1134, IN1–IN2, 1135–1140.

[2] Carle, M.; Pierrat, P.; Lahalle-Gravier, C.; Scherrer, S.; Scherrer, H. Transport properties of n-type $Bi_2(Te_{1-x}Se_x)_3$ single crystal solid solutions ($x \leqslant 0.05$). *J. Phys. Chem. Solids* **1995**, *56*, 201–209.

[3] Yamashita, A.; Tomiyoshi, S.; Makita, K. Bismuth telluride compounds with high thermoelectric figures of merit. *J. Appl. Phys.* **2003**, *93*, 368–374.

[4] Poudel, B.; Hao, Q.; Ma, Y.; Lan, Y. C.; Minnich, A.; Yu, B.; Yan, X.; Wang, D. Z.; Muto, A.; Vashaee, D. et al. High-thermoelectric performance of nanostructured bismuth antimony telluride bulk alloys. *Science* **2008**, *320*, 634–638.

[5] Mehta, R. J.; Zhang, Y. L.; Karthik, C.; Singh, B.; Siegel, R. W.; Borca-Tasciuc, T.; Ramanath, G. A new class of doped nanobulk high-figure-of-merit thermoelectrics by scalable bottom-up assembly. *Nat. Mater.* **2012**, *11*, 233–240.

[6] Finefrock, S. W.; Fang, H. Y.; Yang, H. R.; Darsono, H.; Wu, Y. Large-scale solution-phase production of Bi_2Te_3 and PbTe nanowires using Te nanowire templates. *Nanoscale* **2014**, *6*, 7872–7876.

[7] Drabble, J. R.; Goodman, C. H. L. Chemical bonding in bismuth telluride. *J. Phys. Chem. Solids* **1958**, *5*, 142–144.

[8] Mishra, S. K.; Satpathy, S.; Jepsen, O. Electronic structure and thermoelectric properties of bismuth telluride and bismuth selenide. *J. Phys.: Condens. Mat.* **1997**, *9*, 461–470.

[9] Liu, W. S.; Zhang, Q. Y.; Lan, Y. C.; Chen, S.; Yan, X.; Zhang, Q.; Wang, H.; Wang, D. Z.; Chen, G.; Ren, Z. F. Thermoelectric property studies on Cu-doped n-type $Cu_xBi_2Te_{2.7}Se_{0.3}$ nanocomposites. *Adv. Energy Mater.* **2011**, *1*, 577–587.

[10] Schultz, J. M.; McHugh, J. P.; Tiller, W. A. Effects of heavy deformation and annealing on the electrical properties of Bi_2Te_3. *J. Appl. Phys.* **1962**, *33*, 2443–2450.

[11] Hyun, D. B.; Hwang, J. S.; Shim, J. D.; Oh, T. S. Thermoelectric properties of $(Bi_{0.25}Sb_{0.75})_2Te_3$ alloys fabricated by hot-pressing method. *J. Mater. Sci.* **2001**, *36*, 1285–1291.

[12] Jiang, J.; Chen, L. D.; Bai, S. Q.; Yao, Q.; Wang, Q. Fabrication and thermoelectric performance of textured n-type $Bi_2(Te,Se)_3$ by spark plasma sintering. *Mater. Sci. Eng.: B* **2005**, *117*, 334–338.

[13] Scanlon, D. O.; King, P. D. C.; Singh, R. P.; de la Torre, A.; Walker, S. M.; Balakrishnan, G.; Baumberger, F.; Catlow, C. R. A. Controlling bulk conductivity in topological insulators: Key role of anti-site defects. *Adv. Mater.* **2012**, *24*, 2154–2158.

[14] Starý, Z.; Horák, J.; Stordeur, M.; Stölzer, M. Antisite defects in $Sb_{2-x}Bi_xTe_3$ mixed crystals. *J. Phys. Chem. Solids* **1988**, *49*, 29–34.

[15] Jia, S.; Ji, H. W.; Climent-Pascual, E.; Fuccillo, M. K.; Charles, M. E.; Xiong, J.; Ong, N. P.; Cava, R. J. Low-carrier-concentration crystals of the topological insulator Bi_2Te_2Se. *Phys. Rev. B* **2011**, *84*, 235206.

[16] Fuccillo, M. K.; Jia, S.; Charles, M. E.; Cava, R. J. Thermoelectric properties of Bi_2Te_2Se compensated by native defects and Sn doping. *J. Electron. Mater.* **2013**, *42*, 1246–1253.

[17] Jia, S.; Beidenkopf, H.; Drozdov, I.; Fuccillo, M. K.; Seo, J.; Xiong, J.; Ong, N. P.; Yazdani, A.; Cava, R. J. Defects and high bulk resistivities in the Bi-rich tetradymite topological insulator $Bi_{2+x}Te_{2-x}Se$. *Phys. Rev. B* **2012**, *86*, 165119.

[18] Mavrokefalos, A.; Moore, A. L.; Pettes, M. T.; Shi, L.; Wang, W.; Li, X. G. Thermoelectric and structural characterizations of individual electrodeposited bismuth telluride nanowires. *J. Appl. Phys.* **2009**, *105*, 104318.

[19] Chen, B. L.; Chen, Y. Y.; Lin, S. J.; Ho, J. C.; Lee, P. C.; Chen, C. D.; Harutyunyan, S. R. Fabrication and characterization of electrodeposited bismuth telluride films and nanowires. *J. Phys. Chem. C* **2010**, *114*, 3385–3389.

[20] Shin, H. S.; Jeon, S. G.; Yu, J.; Kim, Y. S.; Park, H. M.; Song, J. Y. Twin-driven thermoelectric figure-of-merit enhancement of Bi_2Te_3 nanowires. *Nanoscale* **2014**, *6*, 6158–6165.

[21] Neuberger, M. *The BiTe-BiSe System Data Sheet*; U.S. Air Force Research Lab., 1966.

[22] Son, J. S.; Choi, M. K.; Han, M. K.; Park, K.; Kim, J. Y.; Lim, S. J.; Oh, M.; Kuk, Y.; Park, C.; Kim, S. J. et al. n-type nanostructured thermoelectric materials prepared from chemically synthesized ultrathin Bi_2Te_3 nanoplates. *Nano Lett.* **2012**, *12*, 640–647.

[23] Zhao, Y. X.; Dyck, J. S.; Hernandez, B. M.; Burda, C. Improving thermoelectric properties of chemically synthesized Bi_2Te_3-based nanocrystals by annealing. *J. Phys. Chem. C* **2010**, *114*, 11607–11613.

[24] Soni, A.; Zhao, Y. Y.; Yu, L. G.; Aik, M. K. K.; Dresselhaus, M. S.; Xiong, Q. H. Enhanced thermoelectric properties of solution grown $Bi_2Te_{3-x}Se_x$ nanoplatelet composites. *Nano Lett.* **2012**, *12*, 1203–1209.

[25] Yoo, B. Y.; Huang, C. K.; Lim, J. R.; Herman, J.; Ryan, M. A.; Fleurial, J. P.; Myung, N. V. Electrochemically deposited thermoelectric n-type Bi_2Te_3 thin films. *Electrochim. Acta* **2005**, *50*, 4371–4377.

[26] Kim, D. H.; Byon, E.; Lee, G. H.; Cho, S. Effect of deposition temperature on the structural and thermoelectric properties of bismuth telluride thin films grown by co-sputtering. *Thin Solid Films* **2006**, *510*, 148–153.

[27] Boulouz, A.; Giani, A.; Pascal-Delannoy, F.; Boulouz, M.; Foucaran, A.; Boyer, A. Preparation and characterization of MOCVD bismuth telluride thin films. *J. Cryst. Growth* **1998**, *194*, 336–341.

[28] Yang, J. Y.; Aizawa, T.; Yamamoto, A.; Ohta, T. Thermoelectric properties of n-type $(Bi_2Se_3)_x(Bi_2Te_3)_{1-x}$ prepared by bulk mechanical alloying and hot pressing. *J. Alloys Compd.* **2000**, *312*, 326–330.

[29] Goldsmid, J. H. *Introduction to Thermoelectricity*; Springer: Berlin, Heidelberg, 2010.

[30] Cutler, M.; Mott, N. F. Observation of anderson localization in an electron gas. *Phys. Rev.* **1969**, *181*, 1336–1340.

[31] Rowe, D. M.; Bhandari, C. M. *Modern Thermoelectrics*; Reston Publishing Company, Inc.: Reston, Virginia, USA, 1983.

[32] Fang, H. Y.; Wu, Y. Telluride nanowire and nanowire heterostructure-based thermoelectric energy harvesting. *J. Mater. Chem. A* **2014**, *2*, 6004–6014.

[33] Fang, H. Y.; Feng, T. L.; Yang, H. R.; Ruan, X. L.; Wu, Y. Synthesis and thermoelectric properties of compositional-modulated lead telluride-bismuth telluride nanowire heterostructures. *Nano Lett.* **2013**, *13*, 2058–2063.

Electronic Supplementary Material

Thermoelectric properties of solution-synthesized n-type Bi_2Te_3 nanocomposites modulated by Se: An experimental and theoretical study

Haiyu Fang[1,†], Je-Hyeong Bahk[2,‡], Tianli Feng[3], Zhe Cheng[4], Amr M. S. Mohammed[2], Xinwei Wang[4], Xiulin Ruan[3], Ali Shakouri[2], and Yue Wu[5] (✉)

[1] *School of Chemical Engineering, Purdue University, West Lafayette, IN 47907, USA*
[2] *Birck Nanotechnology Center, Purdue University, West Lafayette, IN 47907, USA*
[3] *School of Mechanical Engineering, Purdue University, West Lafayette, IN 47907, USA*
[4] *Department of Mechanical Engineering, Iowa State University, Ames, IA 50011, USA*
[5] *Department of Chemical and Biological Engineering, Iowa State University, Ames, IA 50011, USA*
[†] *Present address: Materials Research Laboratory, UC Santa Barbara, Santa Barbara, CA 93106, USA*
[‡] *Present address: Department of Mechanical and Materials Engineering, University of Cincinnati, Cincinnati, OH 45221, USA*

Supporting information to DOI 10.1007/s12274-015-0892-x

S1 Measurement of thermoelectric properties

S1.1 Cross-plane thermal conductivity measurement

The pellets were cut and polished into required dimensions. Seebeck coefficient was measured in home built system by bridging the sample between a heater and heat sink and testing the voltage and temperature difference between the hot and the cold sides in a vacuum chamber. Electrical conductivity was measured with Van der Pauw method in a system where a MMR K-20 temperature stage was used to control sample temperature and an Agilent was connected to provide source current and collect voltage signals. Hall Effect was carried out by applying magnetic field up to 1 Tesla to the electrical conductivity measurement system. The cross-plane thermal conductivity was calculated via the equation $\kappa = \alpha\rho C_p$ (ρ is the density and C_p is heat capacity) and the thermal diffusivity (α) was measured through the laser flush method. All the measurements were carried out under vacuum in the temperature range from 300 to 500 K.

S1.2 In-plane thermal conductivity measurement

The schematic of the experimental setup for characterizing the in-plane thermal conductivity is shown in Fig. S3. The sample was fixed on the aluminum heat sink with silver paste that was also used to connect the

Address correspondence to yuewu@iastate.edu

thermal couple to the suspended end of the sample. To suppress heat convection, the setup was placed in a vacuum chamber with pressure of 2.1–2.3 mTorr. A 1,550 nm laser was used to heat the sample. To enhance laser energy absorption, a black marker was used to paint the sample surface facing the laser. Two lenses were used to enlarge the laser spot before the laser entered the vacuum chamber. Since the laser spot is much larger than the sample size, the laser energy flux hit on the sample surface can be taken as uniform. The heat sink was at room temperature. After laser was applied, the temperature of the suspended sample end rose and it was measured by the thermal couple. The temperature rise is related to the sample's thermal conductivity as $\Delta T = Ql/(2\kappa wd)$. Here, Q is the heating energy, l is the sample length, κ is the thermal conductivity, w and d are the width and thickness respectively. Then the thermal conductivity can be expressed as $\kappa = Ql/(2\Delta Twd)$. To measure the heating energy, a piece of hard and thick paper was placed at the position of the sample. The paper was used to block the laser and a hole sharing the same size of the sample was cut in the paper. The light passed through the hole and a laser power meter (POWER MAX500D) was placed underneath the paper to measure the laser energy. The sample length, width and thickness were measured with micrometer and optical microscope. Then the thermal conductivity of the sample was calculated. The calculated thermal conductivity includes the effect of thermal radiation. The effect of radiation can be calculated as $\kappa_{\text{rad}} = 8\varepsilon\sigma' T^3 l^2/(d\pi^2)$. Here, ε is the emissivity, σ' is Stefan-Boltzmann constant, T is the surface temperature. For the emissivity, the value for the surface facing the laser is 1 and the value for the other surface is estimated to be 0.5, so the average emissivity of the sample is estimated to be 0.75. The maximum effect of radiation is very small (about 3%) so that it would not bring significant error to the final results. The real thermal conductivity of the sample is $\kappa_{\text{real}} = \kappa - \kappa_{\text{rad}}$. To improve the accuracy, one sample was measured for four times with different laser energy and temperature rises. The main error source in this experiment is the laser energy absorption rate, namely the emissivity. The sample surface is coarse and black so the emissivity is taken as 1 in this experiment. The error due to the emissivity is estimated to be 5%. The relative error of the geometrical measurement is estimated to be 1% and the relative error of the thermal couple is also 1%. Therefore, the total relative error of the thermal conductivity is estimated to be 5.4%.

S2 Theoretical modeling

S2.1 Carrier transport modeling

We modeled the carrier transport in the $Bi_2(Te_{1-x}Se_x)_3$ nanocomposites based on the linearized Boltzmann transport equations (BTE) under the relaxation time approximation. The differential conductivity $\sigma_d(E)$ is defined as

$$\sigma_{\text{d}}(E) = e^2\tau(E)v^2(E)\rho_{\text{DOS}}(E)\left(-\frac{\partial f_0}{\partial E}\right) \tag{S1}$$

where e is the electron charge, τ is the total relaxation time, ρ_{DOS} is the density of states, v is the carrier velocity in one direction, and f_0 is the Fermi-Dirac distribution. For the multiple-band transports in $Bi_2(Te_{1-x}Se_x)_3$, the transport properties are calculated by summing all the contributions from each band. The electrical conductivity σ, the Seebeck coefficient S, and the electronic thermal conductivity κ_e are given, respectively, by

$$\sigma = \sum\int \sigma_{\text{d}}(E)\text{d}E \tag{S2}$$

$$S = \sum \frac{1}{qT} \frac{\int \sigma_{\mathrm{d}}(E)(E - E_{\mathrm{F}})\mathrm{d}E}{\sigma} \tag{S3}$$

$$\kappa_{\mathrm{e}} = L\sigma T \tag{S4}$$

where Σ is sum over the bands, q is −e for conduction bands, and +e for valence bands, T is the absolute temperature, and E_{F} is the relative position of the Fermi level to each of the band edge. In fact, the Lorenz number is a function of the Fermi level and band structure, but we found that all the samples in this paper were highly degenerate, so that the Lorenz number can be assumed to be the conventional value, 2.44×10^{-8} W·Ω^{-1}·K^{-2}. More information about the electron transport modeling is found elsewhere [S1].

We included two major conduction bands and two valence bands in our transport modeling, all of which are modeled as non-parabolic bands with 6 band degeneracy each. The band gap, effective masses are all dependent on the Se content, x, found from literature, but assumed to be temperature-independent in this paper. The relaxation time is determined by several major scattering mechanisms in $Bi_2(Te_{1-x}Se_x)_3$. Acoustic phonon deformation potential scattering is a major scattering mechanism for electrons in bulk. In the nanocomposites, we added intense ionized defect scatterings at grain boundaries with the defect density as a fitting parameter to fit the mobility.

S2.2 Lattice thermal conductivity modeling

The calculation of lattice thermal conductivity as a function of electron mobility consists of two steps. The first step is to figure out the average grain diameter for a given electron mobility by using electron grain boundary scattering. The second step is to estimate the thermal conductivity according to the average grain diameter and the phonon-boundary scattering.

S2.2.1 Calculate the average grain diameter

The electron mobility μ and the grain diameter D in the nanocomposites are related by the electron scattering with the Matthiessen's rule

$$\begin{aligned} \frac{1}{\mu} &= \frac{1}{\mu_{\mathrm{imp}}} + \frac{1}{\mu_{\mathrm{def}}} + \frac{1}{\mu_{\mathrm{latt}}} + \cdots + \frac{1}{\mu_{\mathrm{bound}}} \\ &= \frac{1}{\mu_{\mathrm{bulk}}} + \frac{1}{\mu_{\mathrm{bound}}} \\ &= \frac{1}{\mu_{\mathrm{bulk}}} + \frac{m^* v_{\mathrm{F}}}{eD} \end{aligned} \tag{S5}$$

where $1/\mu_{\mathrm{imp}}$, $1/\mu_{\mathrm{def}}$, $1/\mu_{\mathrm{latt}}$, etc., represent electron impurity scattering, electron defect scattering, electron phonon (lattice) scattering, etc., in bulk Bi_2Te_3 with 10% Se. The summation of them gives the reciprocal mobility $1/\mu_{\mathrm{bulk}}$ in the bulk Bi_2Te_3 with 10% Se. The last term $1/\mu_{\mathrm{bound}}$ represents the electron boundary scattering in nanostructured Bi_2Te_3 with 10% Se, which is determined by $\mu_{\mathrm{bound}} = \frac{e}{m^*}\tau = \frac{e}{m^*}\frac{D}{v_{\mathrm{F}}}$. Here m^* and v_{F} are the effective electron mass and the Fermi velocities of electrons, respectively. Based on Eq. S5, the average grain diameter D for a given electron mobility μ is

$$D = \left(\frac{1}{\mu} - \frac{1}{\mu_{\text{bulk}}} \right)^{-1} \cdot \frac{m^*}{e} v_{\text{F}} \tag{S6}$$

For the three carrier concentrations, i.e. 2 × 10^{19}, 9 × 10^{19}, and 1.6 × 10^{20} cm^{-3}, the bulk mobilities μ_{bulk} are 320, 250, and 220 $cm^2 \cdot V^{-1} \cdot s^{-1}$, and the Fermi velocities v_{F} are estimated as 1.5 × 10^5, 2.2 × 10^5, and 2.7 × 10^5 $m \cdot s^{-1}$, respectively. The effective electron mass is $m^* = 0.7 m_0$, with m_0 representing the electron static mass. Based on Eq. (S6), the average grain diameter of samples 5 and 6 are estimated around 4.35 nm. Such grain size reduces the electron mean free path $\Lambda_{\text{e}} = v_{\text{F}} \tau_{\text{bulk}} = \frac{v_{\text{F}} \mu_{\text{bulk}} m^*}{e}$ (24 nm) in bulk Bi_2Te_3 with 10% Se and carrier concentration of 1.6 × 10^{20} cm^{-3} to 3.7 nm in nanostructured Bi_2Te_3 with 10% Se (e.g. samples 5 and 6).

S2.2.2 Calculate the lattice thermal conductivity

Similar to electron transport, the effective phonon mean free path Λ_{p} in nanocomposites is determined by phonon scattering in bulk and phonon-boundary scattering in nano-grains

$$\frac{1}{\Lambda_{\text{p}}} = \frac{1}{\Lambda_{\text{p,bulk}}} + \frac{1}{D} \tag{S7}$$

Based on kinetic theory, the lattice thermal conductivity is $\kappa_{\text{l}} = \frac{1}{3} \int_0^{\omega_{\max}} c(\omega) v_{\text{g}}(\omega) \Lambda_{\text{p,sp}}(\omega) \text{d}\omega = \alpha \Lambda_{\text{p}}$, where α is defined as $\alpha \equiv \frac{1}{3} \int_0^{\omega_{\max}} c(\omega) v_{\text{g}}(\omega) \text{d}\omega$ with ω, c, v_{g} and $\Lambda_{\text{p,sp}}$ representing the phonon frequency, specific heat, group velocity and spectral mean free path, respectively. Based on our previous calculation [S2] and the literature [S3, S4], α is estimated as 5.767 × 10^8 $W \cdot m^{-2} \cdot K^{-1}$. Multiplying Eq. (S7) by α gives the grain diameter dependent lattice thermal conductivity of nanocoposites

$$\frac{1}{\kappa_{\text{l}}} = \frac{1}{\kappa_{\text{l,bulk}}} + \frac{1}{\alpha D} \tag{S8}$$

Here the unknown $\kappa_{\text{l,bulk}}$ represents the lattice thermal conductivity of bulk Bi_2Te_3 with 10% Se and is obtained in the following approach. Samples 5 and 6 have the electrical conductivities of 907 and 829 $S \cdot cm^{-1}$, and thus electronic thermal conductivities $\kappa_{\text{e}} = L\sigma T$ of 0.664 and 0.607 $W \cdot m^{-1} \cdot K^{-1}$, respectively. Their in-plane thermal conductivities were measured as 1.63 and 1.42 $W \cdot m^{-1} \cdot K^{-1}$, respectively. Thus their lattice thermal conductivities are estimated as 0.966 and 0.813 $W \cdot m^{-1} \cdot K^{-1}$, respectively. Sample 5 has a bit larger lattice thermal conductivity is owing to its lower Se concentration and thus less phonon impurity scattering. Since the Se concentration of 10% in our modeling is very close and in between our samples 5 (8.20% ± 0.97% Se) and 6 (11.54% ± 0.68% Se), and the grain diameters of samples 5 and 6 are both around 4.35 nm, thus, the lattice thermal conductivity of our modeling material, i.e. Se concentration of 10%, with grain diameter of 4.35 nm is estimated as $\kappa_{\text{l}} = 0.89$ $W \cdot m^{-1} \cdot K^{-1}$, the average of 0.966 and 0.813 $W \cdot m^{-1} \cdot K^{-1}$. Finally $\kappa_{\text{l,bulk}}$ is obtained as $\kappa_{\text{l,bulk}} = \left(\frac{1}{\kappa_{\text{l}}} - \frac{1}{\alpha D} \right)^{-1} = 1.38$ $W \cdot m^{-1} \cdot K^{-1}$. Since both the constants $\kappa_{\text{l,bulk}}$ and α have been obtained, the lattice thermal conductivity as a function of grain diameter D, or electron mobility μ, can be calculated based on Eq. (S8).

S3 Supplementary figures

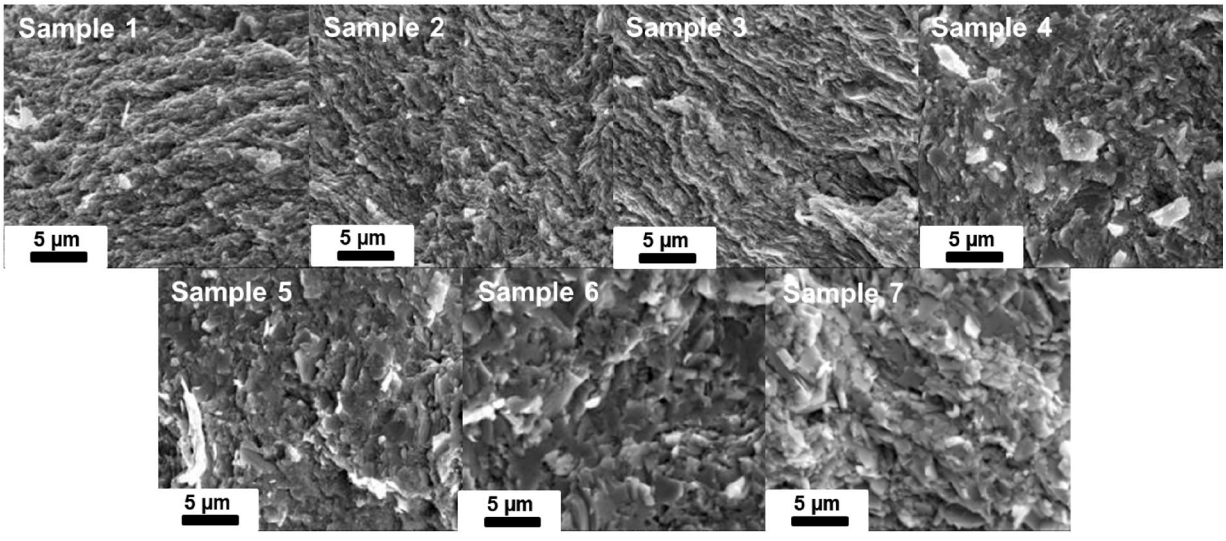

Figure S1 Scanning electron microscope images at the cross section of hot press pellets. Sample ID is labeled on the images.

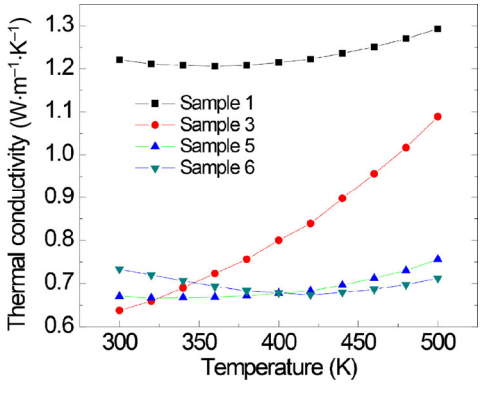

Figure S2 Temperature dependent thermal conductivity of samples 1, 3, 5 and 6 along the cross-plane direction.

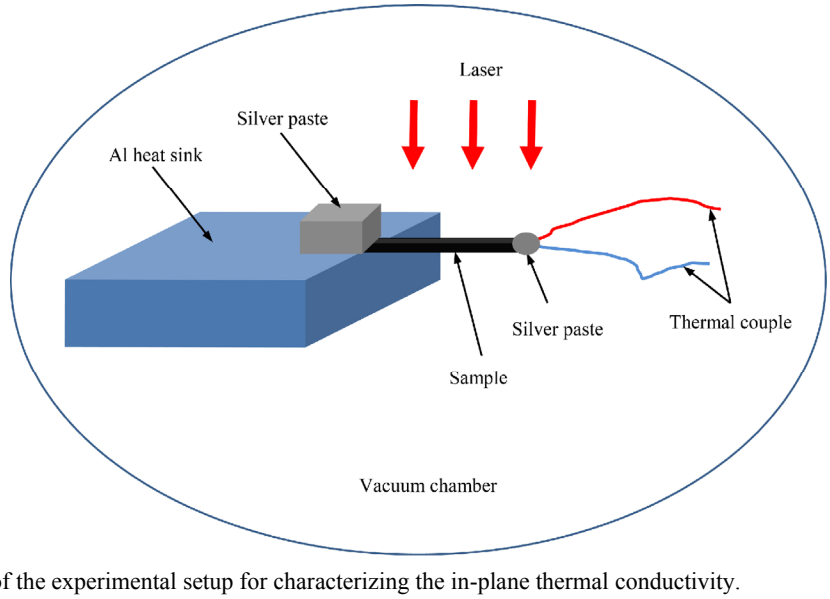

Figure S3 Schematic of the experimental setup for characterizing the in-plane thermal conductivity.

Reference

[S1] Bahk, J.-H.; Shakouri, A. Electron transport engineering by nanostructures for efficient thermoelectrics. In *Nanoscale Thermoelectrics, Lecture Notes in Nanoscale Science and Technology*; Wang, X. D.; Wang, Z. M., Eds; Springer International Publishing: Switzerland, 2014; vol. 16, pp41–92.

[S2] Wang, Y. G.; Qiu, B.; McGaughey, A. J. H.; Ruan, X. L.; Xu, X. F. Mode-wise thermal conductivity of bismuth telluride. *J. Heat Trans.* **2013**, *135*, 091102.

[S3] Mavrokefalos, A.; Moore, A. L.; Pettes, M. T.; Shi, L.; Wang, W.; Li, X. G. Thermoelectric and structural characterizations of individual electrodeposited bismuth telluride nanowires. *J. Appl. Phys.* **2009**, *105*, 104318.

[S4] Hellman, O.; Broido, D. A. Phonon thermal transport in Bi_2Te_3 from first principles. *Phys. Rev. B* **2014**, *90*, 134309.